Ground ice estimation in permafrost samples using industrial Computed Tomography and Multi-Sensor Core Logging and comparison to destructive measurements

Mahya Roustaei [1, 2*], Joel Pumple [1], Jordan Harvey [1], and Duane Froese [1, *]

[1] Department of Earth and Atmospheric Sciences, University of Alberta, Edmonton, Canada
[2] Geotechnics Laboratory, Ghent University, Technologiepark 68, 9052 Zwijnaarde, Belgium

Correspondence to: Mahya Roustaei (mroustae@ualberta.ca) or Duane Froese (duane.froese@ualberta.ca)

Abstract.

Permafrost contains a variety of ground ice types (e.g., pore, segregated, intrusive, vein, or massive ice) that have a diversity of cryotextures which organise to form distinctive cryostructures. The distribution and abundance of those ground ice types determines the potential for thaw subsidence and terrain effects of permafrost landscapes. Analysis of permafrost samples allows improved understanding of ground ice formation, internal and external permafrost processes, and improved tools to predict thaw settlement and consolidation. However, most methods to characterise permafrost are destructive and of low resolution. Here, some of the limitations of traditional destructive methods are overcome using an industrial Computed Tomography scanner (CT). We use this laboratory-based method to systematically characterize five permafrost samples. We visualise cryostructures, measure frozen bulk density, and estimate volumetric and excess ice contents non-destructively and compare these results with traditional destructive analyses at similar spatial scales.

The results show strong agreement between traditional destructive analyses (RMSE's for density, VIC, and EIC are 0.12 g/cm3, 3% and 6%, respectively) as well as recent developments using a Multi-Sensor Core Logger (MSCL) (RMSE's for density and VIC are 0.08 g/cm3 and 7%, respectively). These results demonstrate that these non-destructive approaches can produce consistent results, and provide the added benefit of archiving images and enhancing digital permafrost datasets. Development of standardised and interoperable methods for permafrost characterization has the potential to build more robust permafrost datasets and strengthen efforts to understand future thaw trajectories of permafrost landscapes.

1 Introduction

Permafrost is rock or soil that has remained below 0°C for at least two consecutive years. Within permafrost, several different types of ground ice can form: pore ice within the void spaces between soil or rock particles; segregation ice as distinct lenses formed through migration of water within permafrost; aggradational ice, a type of segregation ice, that forms as the permafrost table rises; vein or wedge ice that forms within thermal contraction cracks; intrusive ice that forms when water is injected under pressure; or massive ice that refers to relatively pure bodies of ice within permafrost. (Subcommittee onPermafrost., 1988). These differing types of ground ice have distinctive associations of cryotextures, which refer to the appearance and characteristics of ice crystals, gas bubbles and their interfaces with soil particles at a more microscopic scale; and cryostructures which refer to the three-dimensional patterns and arrangements of ice bodies within the frozen ground (such as layered, lenticular, or reticulate patterns) (Murton and French, 1994; French and Shur, 2010). Taken together, these ice-related features help identify the genesis of perennially frozen sediments and can provide insights into the conditions under which the permafrost formed, which can aid in understanding potential ground ice distribution. Of particular importance is excess ice – or ground ice that exceeds the natural pore volume that the sediment would have under unfrozen conditions (Brown et al., 1997; Zhang et al., 1999; Cai et al., 2020; Van Everdingen, 1998). When excess ice melts, it causes thaw settlement and ground subsidence, making its quantification increasingly critical as warming temperatures degrade permafrost across permafrost regions (e.g. Kokelj et al., 2024). Projections of widespread permafrost thaw by the end of this century (e.g. Cai et al., 2020) highlight an urgent need for standardised methods to measure and map excess ice distribution to better predict future landscape changes.

Cryostructural approaches to ground ice classification, building on Russian literature, particularly Katasonov's (1969, 1978) cryofacies methods, focus on understanding permafrost genesis and development through systematic analysis of the shape, size and spatial patterns of ice inclusions in frozen ground. This approach contrasts with the more commonly used North American engineering-focused descriptive systems developed by Pihlainen and Johnston (1963) and Johnston (1981), which rely primarily on visual descriptions and simple field tests, such as thawing samples to observe supernatant water content similar to the method described in Kokelj and Burn (2003). While the descriptive approach provides practical field-based classifications useful for engineering applications, the cryostructural approach offers more process-based insight into permafrost formation processes and potential ground ice distribution, which is increasingly important for predicting thaw settlement and landscape response to climate warming.

Traditional approaches to permafrost characterization, whether using more descriptive engineering-oriented approaches (Pihlainen and Johnston, 1963; Johnston, 1981) or more detailed cryostructural classifications (Murton and French, 1994; French and Shur, 2010), rely heavily on visual description of exposures and cores (Kanevskiy et al., 2011; Stephani et al., 2014). While these approaches have advanced our understanding of permafrost, they require substantial experience of the

analyst, and are difficult to standardise. Quantitative methods typically require destruction of samples to measure ice and moisture contents, which works well for ice-rich mineral soils but presents challenges for organic-rich materials where water may be retained in thawed samples. These limitations have driven the development of non-destructive methods like Computed Tomography (CT) scanning that can systematically analyse intact frozen cores, providing standardised, quantitative data on ground ice while preserving samples for additional analyses. This approach offers the potential to better understand permafrost formation, internal structure, and likely response to thaw while developing more consistent and interoperable methods applicable across different permafrost materials.

Micro-computed tomography (μCT) has emerged as a promising solution to the limitations of traditional permafrost characterization methods since the pioneering work of Calmels and Allard (2004, 2008), who demonstrated its utility for measuring ice and gas contents in permafrost and linking these to processes of ground ice formation. Subsequent studies have expanded the application of CT scanning to examine cryostructures (Calmels et al., 2010; Fan et al., 2021), excess ice (Lapalme et al., 2017), soil degradation in freeze-thaw cycles (Nguyen et al., 2019; Wang et al., 2018, 2017; Roustaei et al., 2022, Roustaei et al., 2024), quantification of micro-lenticular ice lens formation (Darrow and Lieblappen, 2020), unfrozen water content (Roustaei et al., 2022), soil-ice relations (Torrance et al., 2008), and permafrost composition (Nitzbon et al., 2022).

However, despite these advances, there have been few systematic comparisons of high-resolution CT scanning (< 100 μm) with established methods for differentiating excess ice from pore ice across different permafrost materials. This study addresses this gap by using industrial CT scanning, which offers higher peak power and resolution than medical CT scanners, to analyse five different permafrost cores representing a range of typical properties. We develop a new approach using an internal water standard to calibrate linear attenuation coefficients to real density values, and systematically compare CT-derived measurements of frozen bulk density, excess ice, and volumetric ice contents with both destructive physical measurements and Multi-Sensor Core Logging (MSCL) results from Pumple et al. (2023). We include a sensitivity analysis to examine how spatial resolution affects excess ice estimation. While our sample set does not capture the full heterogeneity of permafrost materials and ground ice abundance, it provides a rigorous test of CT methods for quantifying ground ice in common permafrost materials, with the goal of developing more robust and standardised approaches for permafrost characterization and mapping.

2 Methods and Materials

2.1 Field site and coring

Five cores were compared in this study, each representing common materials encountered in permafrost regions and containing a relatively simple vertical cryostratigraphy to minimize the impact of lateral heterogeneity (Table 1). Lateral heterogeneity would cause noise in our results when comparing multiple data acquisition methods within the same material but not identical sample volumes (Figure 1). This effort is explained further by Pumple et al. (2024).

These cores were collected as a result of two separate field campaigns during the summers of 2013 and 2019. Following extraction, the cores were bagged, labelled and stored at subzero temperatures via a pre chilled cooler and quickly transported to the field base where a chest freezer was present. The chest full of cores was then transported to the Permafrost ArChives Science (PACS) Laboratory. The samples were then archived into the PACS Lab walk-in archive freezer space. PACS Laboratory hosts a specialized imaging space where both the Nikon XTH 225 ST and the Geotek multi-sensor core logger (Pumple et al., 2024) are located. The imaging space is kept at 23 °C and as a result, special consideration has to be taken when working with frozen materials. An insulated sample container was used to keep the samples frozen during the scanning process discussed further in section 2.3.

2.2 Sampling Process

In this study the samples were prepared for two different stages; non-destructive scans and destructive physical measurements. We took considerations in both stages to ensure the destructive and non-destructive results were comparable. As such for the non destructive scans, physical cores were cut in half and run through all non-destructive data collection methods. For the second stage, a duplicate transect of cuboid samples was collected from the middle of the core to allow non-destructive data analysis at a higher resolution on one set of the subsampled cubes. As seen in Figure 1, this resulted in the cuboids flanking either side of the MSCL and CT results which were collected from a central transect on the half-core samples.

2.3 Industrial Micro Computerised Tomography

Micro Computed tomography (μCT) was used to examine the ice, sediment, and gas contents of several permafrost cores and cube samples. This method is a non-destructive technique that has been useful in the investigation of geological porous media (Ashi, 1997; Ketcham and Carlson, 2001; Kozaki et al., 2001; Flisch and Becker, 2007; Calmels and Allard, 2004; Van Geet et al., 2005; Tanaka et al., 2010; Nitzbon et al., 2022). This imaging method captures radiograph images through the production of x-rays which pass through a cabinet and are recorded by the detector panel opposite the source. The sample is placed between the source and the detector panel and the resulting relative absorption of the x-rays energy is recorded by the detector panel creating the radiograph image. To collect a 3 dimensional image a set of two-dimensional X-ray radiographs are collected at multiple angles, and secondly reconstructed to form a 3D image. The final measurement unit which is commonly visualised

in a histogram is the linear attenuation coefficient which depends on both the density and the electron density of the material (Ketcham and Carlson, 2001). This study differs slightly from earlier permafrost CT studies that report values in Hounsfield units that are common in medical CT studies (eg. Calmels et al., 2010). In this study, an internal calibration process is used to convert the primary linear attenuation values derived from the CT data directly to density (g/cm^3).

The scans presented here were captured using a helical scan with a Nikon XTH 225 ST cabinet-based industrial computed tomography micro-CT scanner. The system uses an electronically adjustable 225Kv 225W power source (Figure 2). This system includes both a tungsten rotating reflection target source and a tungsten fixed reflection target source coupled with a 16-bit 2000x2000 pixel detector capable of a focal spot size range of 3-121 µm depending on the size of the area of interest and size of the object being scanned. The 10 cm diameter frozen permafrost half cores were scanned with the reflection target source at 200 Kv 35 µa with an exposure time of 125 ms and a voxel (3D volume element representing pixel resolution and slice thickness) size of 65 µm. Scan times ranged from 30 to 45 minutes per core, with a maximum height of ~12 cm scanned per core due to vertical stage movement limitations and inclusion of calibration materials. The subsampled cubes from the cores were scanned with the rotating reflection target source at 225 Kv 133 µa with an exposure time of 125 ms and a voxel size of 25 µm. Scan times for the subsampled cubes were 30 minutes per cuboid. The images were reconstructed into three-dimensional grey-scale volumes using the Nikon CT pro 3D software and analyzed using ORS Dragonfly 2022 image processing software (ORS 2021).

This project was completed during development of an insulated sample holder for use in the CT scanner. Both cubes and cores were housed in the same style of a styrofoam container, however, the internal setup varied due to the size of the sample under investigation. Cores were taken from a nearby chest freezer, quickly placed in a larger styrofoam container with an inner diameter of 12 cm in the vertical position and an ice pack was placed directly above them (Figure 2B and C). For this experiment, all ice packs were cooled to -80 C prior to being added to the container at the start of the scan.The cubes were held in a slightly smaller container with an inner diameter of 9 cm in a small plastic vial with a foam divider directly above (Figure 2D). The cubes were cooled with a small amount of dry ice placed on a perforated foam divider to bathe the underlying sample with cold air during scanning. Both setups are able to hold the core's surface temperatures below freezing for the full duration of the scan time.

It should also be noted that the partial results for most full cores are due to a height restriction encountered during the helical scans. Although the CT scanner can hold samples up to ~ 30 cm wide by 35 cm high, the area that is able to be scanned is dependent on the desired voxel size and the width of the sample. This restriction was resolved after cores were subsampled for the destructive method. This means for some of the cores we were unable to compare the complete vertical data sets of the MSCL, destructive, and CT results (e.g. peat core).

2.3.1 CT Calibration

The linear attenuation coefficient (μ) represents the energy attenuated within a single voxel volume while the voxel population is the population of voxels within a scan volume (Ketcham & Carlson, 2001). By creating a histogram (linear attenuation coefficient vs voxel population) with these values, distributions of relative grey values can be presented. If uncalibrated, the resulting grey values observed in the histogram of a CT scan appear as linear attenuation coefficients. The medical field has developed methods for converting linear attenuation coefficients to Hounsfield units and as a result, the Hounsfield unit has become commonly used in CT research (Hounsfield, 1973; Wellington and Vinegar, 1987; Duliu, 1999; Knoll, 2000; Ketcham and Carlson, 2001; Duchesne et al., 2009). Lee et al., 2015 took it one step further and converted mean Hounsfield unit values to bone mineral density values (mg/cm^3) via a linear regression analysis. A similar approach was used in this study by collecting the CT scans with an internal standard of known density (water) later used to calibrate the resulting linear attenuation coefficients into g/cm^3 using the Nikon CT Pro 3D software. It should be noted that all cores were scanned with ice, water, and aluminum calibration pieces of which water proved to be in closest agreement with destructive analyses. The water and aluminum were located outside of the insulated container during the core scans to avoid freezing. The cube scans had only the water located directly above the cube sample but isolated from the sample and dry ice by insulated foam to minimize the exposure to the cold air temperature within the insulated container. The aluminum calibration piece generally underestimated the bulk density while the ice calibration piece resulted in a slight overestimation. Aluminum was chosen for its consistent density of 2.71 g/cm^3 representing an upper limit of the expected bulk density within the selected materials. The ice calibration was a 15 ml falcon tube filled and frozen at -5C to minimize expansion issues and bubbles. Overall the water calibration produced the most accurate results apart from ice-poor sediments. The Nikon CT Pro 3D software uses a linear two-point calibration with the first fixed point being air (equal to zero) and the second a user-defined value based on a user-selected pixel population. A representative (local) population of pixels was selected from our water sample in a 2D slice of the scan and informed the expected average target value (1 g/cm^3). This results in displaying grey values in g/cm^3. These densities can then be presented in a histogram where the shape of it changes with the proportion of the component materials and thus approximates the volumetric content in a sample (Calmels et al. 2010).

2.3.2 Image Processing

Image preprocessing usually consists of two main stages; 1) selection of the Region of Interest or (ROI), 2) segmentation. In this study both stages were done using Dragonfly software (ORS 2021). This software enabled us to process the three-dimensional reconstructed X-ray tomographs of the frozen materials to segment, quantify, calculate, and illustrate the cores' physical properties. For the first stage, a series of ROIs were created in the half core CT results down the central vertical axis of the cores to mimic the data collection points of the MSCL as presented in Pumple et al. (2024). Figure 1 displays the relative location of these ROIs which were sized to match the spot size of the gamma-ray at the surface of the core, ~10 mm in diameter. The central point of each ROI was placed 5 mm apart resulting in a significant overlap between adjacent data points, again

similar to the data collection process for the MSCL. In this study, all cores were calibrated so the histogram values were displayed in g/cm^3. To extract the frozen bulk density from each ROI, the mean grey values were extracted in calibrated density values (g/cm^3).

The second stage, segmentation or the ability to differentiate materials, depends on their respective linear attenuation coefficients, meaning materials with divergent densities and/or atomic numbers are easier to differentiate (Kyle and Ketcham, 2015). Analysing a multi-modal histogram of a CT image is straightforward for material differentiation while materials with narrow unimodal density distributions close densities appear as a single peak in the histogram. In addition to the relative density of the scanned materials, the image resolution or voxel size also directly impacts the image segmentation process. The voxel size can impact the image segmentation through the partial volume effect which relates directly to the resolution or voxel size of the scan and for geological samples, grain size, minimal pore size, and organic content (Soret et al., 2007; Nitzbon et al., 2022).

In this study, an automatic image thresholding method named "Otsu " was used. The algorithm of this method, proposed by Nobuyuki Otsu (1979), performs automatic clustering-based image thresholding, assuming that there are two classes of pixels which are "*foreground*" and "*background*" pixels of the image. The optimum thresholding is calculated by distinguishing the two classes so that the minimum class variance is obtained (Kumar and Tiwari, 2019). This method was applied to the selected regions of interest from stage one to differentiate sediment and ice. In each image processing step, we tried to isolate the materials within our scans based on density and slowly slice away the lighter density portion (ice) until we are certain we have collected the target material range (often a mixture of ice and sediment). Figure 3 shows the ice (less dense material) being segmented from the surrounding sediment through multiple image processing steps using the Otsu method where only the background (less dense) portion of the previous step is added to the final result. This approach shows that applying the first image processing step will mainly extract the visible ice while using multiple Otsu analyses additional lower-density ice-rich mixtures (mainly pore ice) are extracted, e.g., the area shown inside the red circle of Figure 3B-D. Note that all the above mentioned segmentation steps can also be done by visual inspections instead of automatic thresholding method but it can vary significantly between users, leading to inconsistent results.

2.4 Physical Density Measurements

Ground-ice content is typically expressed either as the *gravimetric moisture/ice content* (the ratio of the mass of the ice in a sample to the mass of the dry sample) or the *volumetric moisture/ice content* (the ratio of the volume of ice in a sample to the volume of the whole sample) (Van Everdingen, 1998) while excess ice refers to the amount of ice in the soil that exceeds the volume of the pore space in the unfrozen state. Similar to thaw-strain measurements in geotechnical investigations (Crory, 1973; Shur, 1988; Pullman et al., 2007; Kanevskiy et al., 2012), Kokelj and Burn (2003) and O'Neill and Burn (2012) both applied a method for destructively extracting excess ice content measurements from frozen samples. This method includes the

complete thaw, homogenization, and settling time of the sample to extract the supernatant water content and estimate excess ice content. Their method does not require measurement of frozen sample volume since the volumes of sediment as well as the supernatant water should be recorded from the beakers containing the samples once completely thawed. The excess ice content (E_i) of the samples can then be estimated by the equation (Kokelj and Burn, 2003):

$$(Ei) = \frac{(Wv*1.09)}{(Sv+Wv*1.09)} * 100 \quad (1)$$

where *Wv* is the volume of supernatant water (cm^3), multiplied by 1.09 to estimate the equivalent volume of ice, and *Sv* is the volume of saturated sediment (cm^3).

This study takes an approach similar to Kokelj and Burn (2003) in that the supernatant moisture content is destructively assessed in order to calculate excess ice content. However, since the volume of soil samples was precisely measured through the following steps (Pumple et. al, 2024), volumetric ice contents were also measured.

To independently assess density and ice content measurements and also being able to perform scans at higher resolutions, the cores were subsampled as 2x2x4cm cubes. The subsampling process was done in a walk-in freezer maintained at −7°C. The initial step involved removing material from the outer edges of the whole core that might have thawed during coring or been affected by sample storage. Core segments were split lengthwise with a rock saw equipped with a 35 cm diameter diamond-cutting wheel. Cuboid aliquots were cut from one half of the split core, while the other half was retained as an archive. The rounded edges were removed from the half core to expose an internal slab. For this study, a duplicate set of cuboids was obtained by cutting the internal slab in half. Approximately 3 cm^3 aliquots were subsampled from the cores to ensure that the cuboids did not fracture or disintegrate during sampling due to the lower ice content. Digital callipers (±0.01 mm) and a digital analytical balance (±0.01 g precision) were used to measure physical dimensions and mass, respectively, to calculate the frozen bulk density. The cuboids were then thawed at room temperature for 24 hours in glass beakers covered with Parafilm to minimize evaporative loss. Excess moisture was removed from the beakers containing the thawed samples, and the sample weight was recorded again to calculate excess moisture content. The cuboids were then dried in an oven for 24 hours at 105°C and reweighed to determine both volumetric ice content and gravimetric moisture content. Finally, the remaining dried material was heated at 550°C for 4 hours to determine the percent organic content via loss on ignition. High organic content could result in water absorption by soil matrix upon thaw and more complexity in measuring excess ice contents.

Because in some soils, such as peat, excess ice will be absorbed by the soil skeleton upon thaw (Johnston, 1981), the Kokelj and Burn method was adjusted for samples with high organic contents by applying a slight pressure on the thawed cube and extraction of the released water. Additionally, the organic content of each sample was measured via loss on ignition (LOI) (Heiri et al., 2001). The *cuboid* method, described by Bandara et al. (2019), is similar to other volumetric and gravimetric methods used to measure bulk density and ice content, but takes advantage of the frozen state of the material which allows for a greater degree of sampling precision. Processing is undertaken in a walk-in freezer following methods outlined in Pumple et al. (2024).

2.5 Multi Sensor Core Logger (MSCL)

The PACS Laboratory MSCL is a floor-mounted, automated logging system, manufactured by Geotek, which can be used to analyse whole or split cores. This core logger is equipped with two magnetic susceptibility instruments, a line-scan camera, and a Caesium-137 (^{137}Cs) gamma source and detector which provides measurements of gamma attenuation. Pumple et al. (2024) provides additional details on the methods used for the MSCL data collection and calibration. The combination of the frozen bulk density results from the gamma attenuation, an estimation of soil density, and the equation presented for volumetric ice content, following Lin et al. (2020), can be used to estimate non-destructively using the MSCL (Pumple et al., 2024).

3 Results and Discussions

Figures 4 A and B show one slice of a small ROI and its histogram from 5 different cores of this study. The differences in the shapes of the histograms are due to the different sediment densities. The diamicton core has the highest sediment density and a bimodal histogram in which the first mode represents ice and the second is related to the sediments and clasts. Whereas in the other cores, ice and sediment appear as a single mode. Image segmentation of these slices using the Otsu method resulted in the differentiation of 5 different classes of ice/sediment ratios on the basis of their relative densities; air, low ice, high ice, low sediment, and high sediment shown in Figures 4 B and C. Low ice comprises primary visual or excess ice while high ice mainly results from extraction of pore ice or ice proximal to sediment (sediment-rich ice). It should be noted that the pore ice inclusions within the mineral soil matrix are often smaller than the spatial resolution of the CT and the resulting grey value of a voxel is then a mixture of low-density ice and high-density minerals. This phenomenon, called partial volume effect, is the main reason why the high ice appears denser. Low sediment and high sediment are also differentiating ice-rich sediments and sediments with lower and higher densities, respectively. Figure 5 illustrates the image segmentation results in the whole diamicton core.

3.1 Core Results

Physical properties of the permafrost samples, determined from the cuboids, including frozen bulk density, volumetric (VIC) and excess ice contents (EIC), and organic contents are plotted versus the depth of the cores and shown as B, C, and D in Figures 6-10, respectively. The vertical cross-section photo of the core (A) is also presented in these figures. The non-destructive CT results for VIC, EIC, and bulk density for each core are then compared to both the destructive cuboid and non-destructive MSCL results using an average root mean square error (RMSE) (Table 2).

3.1.1 Ice-rich Silt Core (BH18-211):

Figure 6 shows the destructive (cuboid) and non-destructive (CT and MSCL) results of the ice-rich silt core, illustrating that the CT frozen bulk densities are in strong agreement with both the cuboid (RMSE = 0.12 g/cm^3) and MSCL (RMSE = 0.14 g/cm^3) results. This core has a high organic content (8-19% organic), micro-lenticular and layered cryostructures, and 66% silt. Cuboid physical EIC and VIC measurements range from 19-34% and 68-76%, respectively, while the CT EIC and VIC estimates range from 20-68% and 32-74% at the same depths where cuboid measurements were collected. The 65 µm EIC (redline in Figure 6C) shows good accordance with the cuboid EICs (RMSE = 9%) apart from the ice layer where the cuboid's relatively low sample resolution results in an averaging out of the ice content across the ice layer. The 65 µm CT-VICs (black line in Figure 6C) illustrate the resolution limitation in extracting the pore ice of this sandy silt core while the 25µm VICs shown as black cubes in the same plot tackle this limitation and agree well with VICs extracted from the Cuboid method (RMSE = 7%). The MSCL VICs follow the same trend as the cuboid data (Fig 6-C) but consistently tend toward lower values in the ice-poor regions.

3.1.2 Transition Core (BH12F-138):

Figure 7 shows the results of the transition core from both destructive (cuboid) and non-destructive (CT and MSCL) methods, illustrating a sharp boundary between an ice-rich silty peat, containing massive and rare crustal cryostructures, and an ice-poor inorganic silt with a mainly micro-lenticular cryostructure. The organic content of the core's top section, ranging from 53-71%, highlights this transition (Figure 7D). Cuboid physical EIC and VIC measurements range from 6-28% and 64-88%, respectively, while the CT EIC and VIC estimates range from 9-33% and 42-95% at the same depths where cuboid measurements were collected. This figure also shows that the CT bulk density results are in strong agreement with both the cuboid (RMSE = 0.13 g/cm^3) and gamma attenuation data (RMSE = 0.06 g/cm^3) (Pumple et al., 2024). The 65 µm EIC results (red line in Figure 7-C) follow the cuboid results (RMSE = 5%) in the silty section. The 65 µm VIC (black line in Figure 7C) resolves more than 50% of pore ice, while the higher resolution (25 µm, black cubes in Figure 7C), estimates up to 100% (RMSE = 3%).

3.1.3 Diamicton Core (BS19-3-6):

Figure 8 illustrates the destructive (cuboid) and non-destructive (CT and MSCL) results of the diamicton core. This ice-rich diamicton contains both suspended and crustal cryostructures and more than 50% silt (Table 1). Overall the bulk density and ice measurements from CT display high concordance with the gamma attenuation (RMSE = 0.14 g/cm^3), and cuboid (RMSE = 0.14 g/cm^3) methods (Figure 8). Cuboid physical EIC and VIC measurements range from 30-50% and 48-66%, respectively, while the CT EIC and VIC estimates range from 22-57% and 36-77% at the same depths as the cuboid measurements. The 65 µm EIC results (red line in Figure 8C) follow the cuboid results (RMSE = 8%). The only point where the datasets differ notably is at 2-4 cm depth where the MSCL values shifts towards lower densities due to the core's lateral heterogeneity while the CT

density still lines up well with the cuboid results. The ice contents of this cube are also much lower than CT and MSCL results. This is due to the collection procedure of the cubes which were just off-center to accommodate a duplicate run of cubes down the middle of the core for CT imaging and destructive measurements (as shown in Figure 1). This single cube highlights the effect of differences in the locations of ROIs between CT/MSCL and the cuboid methods. Moreover, at this depth in the core cuboid sample, there was a clast which resulted in a local density high and lower ice content.

In this core, the 65 μm VICs agree well with the cuboid-VICs, MSCL (RMSE = 4%) ice contents, and 25 μm cube scan results (RMSE = 3%) while in the transition core, the 65 μm VICs underestimated the other VIC results. The difference between the 65 um VIC results and other VIC results for all cores except the diamict could be a result of the sample's grain size as the diamict has high clay content (~18%) relative to the other cores (~8-12%) (Table 1).

3.1.4 Ice-poor Silt Core (BH20B-337):

Figure 9 shows the results of the ice-poor silt core from both destructive (cuboid) and non-destructive (CT and MSCL) methods, illustrating a massive (non-visible) cryostructure within this inorganic silt that highlights the relatively low overall ice content throughout the core. This core has little variability throughout its profile. The CT bulk densities are consistent with both the cuboid (RMSE = 0.14 g/cm^3) and gamma attenuation data (RMSE = 0.14 g/cm^3) (Figure 9). The 65 μm EIC results compare well with the cuboid EIC results (RMSE = 5%) while the 25 μm cube scan ice contents show strong agreement (RMSE = 3%) with the volumetric cuboid ice content estimates. It should be noted that based on the EIC results of 65 μm scans, the core has a small percentage of ice (around 5%) in the form of microstructures beyond the natural pore space within the host sediment. However, upon thawing, the surrounding sediment absorbs the moisture into the available pore space, resulting in no EIC during the destructive analysis.

3.1.5 Peat Core (DH13-589):

Figure 10 illustrates the destructive (cuboid) and non-destructive (CT and MSCL) characterization results of the peat core, with little variability throughout its profile. The core is formed of homogenous organics, with an organic-matrix cryostructure of visible ice within the densely packed peat. The CT bulk density results are similar to both the cuboid (RMSE = 0.05 g/cm^3) and gamma attenuation results (RMSE = 0.03 g/cm^3) (Figure 10). The 65 μm ice content results (39-48% of EIC) are also in accordance with the cuboid excess ice results (RMSE = 4%). The 65 μum and 25 μum VICs are both showing good estimates of VICs (RMSE = 1%). It should be considered that the adjusted method for extraction of supernatant water, using slight pressure to release water from the organic matrix, was applied to the cubes of this core. As it was previously discussed, this pressure will release the excess water that was absorbed by the peat skeleton upon thaw (Johnston, 1981).

3.2 Sensitivity analysis

In this study in order to do a sensitivity analysis and investigate the impact of resolution on the delineation between ice and sediment, repeat scans were conducted on the same cube. Initially, the half cores (10 cm diameter) were scanned with a 65 μm voxel size. This was due to the physical size (width) of the imaging window. The smaller size of the cubes, however, presented an opportunity to collect data from the same material but at a resolution of 25 μm. Some of the cubes were also scanned at the same 65 μm resolution as the half cores to make a direct comparison. Figure 11 shows the same slice location and orientation from the same cube at two different resolutions.

A ROI, shown as a red square in Figure 11, was then selected in each cube scan to make a direct comparison between the delineated (Otsu split) ice contents from image processing and the ice contents determined from the cuboid results. As reference points, the cuboid ice content results for this cube were as follows; 22% EIC and 65% VIC. Figure 12 shows the collected data from repeat image processing steps using the Otsu method of each cube as well as the cuboid results. The initial image processing steps for both the 25 μm and 65 μm scans closely capture the expected value of the EIC. However, only the 25 μm cube captures a representative value relative to the cuboid data for the expected VIC. This value is reached after 6 image processing steps using the Otsu method. These results illustrate the sufficiency of 25 μm resolution in extracting trapped ice inside pore spaces of this sandy silt sample which could be due to the smaller size of pores than the resolution. The nature of the curve suggests that VIC cannot be delineated from the 65 μm resolution scans however EIC is possible.

Additionally, there is an observable increase in the amount of pore space or gas captured in the 25um resolution relative to the 65um. This difference highlights the 25um scan's increased potential to capture, and as a result segment, the different components within the scanned material.

3.3 Comparison of CT and Cuboid Density and Excess Ice Results:

Segmentation of the CT images using the Otsu method allows comparison of CT-derived bulk densities, excess ice, and volumetric ice contents with estimates from the cuboid method at similar resolution. We completed these comparisons at 65 μm and 25 μm (Figures 13, 14 and 15). These figures display good agreement for density, excess ice, and volumetric ice measurements with RMSE of 0.12 g/cm^3, 6%, and 3%, respectively. Additionally, the CT results compare well with the MSCL results for both density and VIC with RMSE's of 0.08 g/cm^3 and 7%, respectively (Figures 16 and 17). The differences between the estimated EICs from CT image processing (65 μm-whole core) and the measured ones from the cuboid method are due to the differing resolutions, i.e., 0.5 cm for CT and 2 cm for the cuboid method, as well as the different locations of the regions of interest (previously described in section 2.2). The strong accordance of the VICs highlights the opportunity for higher resolution scans to estimate pore ice.

3.4 Comparison of Non-destructive Methods:

The results of this study show strong agreement between the two non-destructive methods: CT and MSCL and highlight the importance of continued development and refinement of non-destructive methods for extracting physical properties from permafrost materials.

The presented CT method allows for whole core high-resolution (65 μm) three-dimensional imaging of cores, measurement of bulk density and estimation of excess ice contents at a user-defined scale. This contrasts with MSCL which is restricted to a fixed data collection transect down the center of the core (~ 1cm wide) with a maximum sample resolution of ~ 0.5 cm, high resolution (25 μm) 2-dimensional half-core images and currently provides only volumetric ice estimates, and no direct estimates of excess ice. The CT method is capable of estimating volumetric ice contents but requires cores to be subsampled to a smaller size (2x2x4 cm cube) to allow for finer resolution scans (25 μm).

It is worth noting that the MSCL provides a more rapid method for collecting bulk density and volumetric ice content estimations in comparison with the CT method. However, in addition to bulk density and volumetric ice content estimations, the CT method can provide direct estimates of excess ice content. Visible ice can be segmented and isolated from the remaining sediment and pore ice when scanning split cores at 65 μm voxel size, allowing the opportunity to better estimate EIC values compared to MSCL methods. Therefore, in terms of a non-destructive method for identifying and quantifying excess ice within permafrost cores the CT method provides a more robust approach although the image processing and acquisition costs are significantly greater.

4 Conclusions

This study investigated the application of high-resolution industrial CT scanning as a non-destructive method to tackle the limitations of traditional destructive methods (e.g., visual acuity, poor reproducibility, and low resolution) in permafrost characterization. Investigations were done by systematically logging permafrost cores, visualising cryostructures, measuring bulk density, and estimating volumetric and excess ice contents, independently. Five permafrost cores, representing common materials encountered in permafrost regions, were scanned at voxel sizes of 65 and 25 μm. A new calibration method was used to extract real densities in g/cm^3 directly from CT images. Image segmentation results using Otsu automatic image thresholding method illustrated the effectiveness of this method in generating robust segmentation results while the visual inspection method has its own drawbacks, e.g. inspector's visual acuity and poor reproducibility.

The initial identification of different materials from CT images showed 3 classes; air (gas), ice, and sediments while image processing steps of the scans (using Otsu method) illustrated significant density differences in ice and sediment classes. Image segmentation results using multiple image processing steps showed visual/excess ice as a lower density relative to the pore ice and delineated two sediment classes based on densities.

Since manual and visual thresholding is subject to operator experience and judgement and also not applicable in images with unimodal histograms related to materials with close densities (organic materials and ice), an automatic thresholding technique was used in this study to generate more consistent results.

Comparison of the image processing results and extracted physical properties of 5 permafrost cores were validated against a destructive method (cuboid) and MSCL non-destructive method. The results showed strong agreement between these three methods (CT and cuboid) considering their differing resolutions and regions of interest with overall average RMSE's of 3%, 6% and 0.12 g/cm^3 for VIC, EIC and density, respectively. This agreement demonstrates the applicability and reliability of non-destructive methods in tracking physical and cryostructural details of permafrost cores and producing replicable, cost-effective measurements. A sensitivity analysis of the impact of differing resolutions on the delineation between ice and sediment showed that higher resolution scans generate more accurate VICs while the lower resolution scans are still sufficient for estimation of EICs and a rough estimation of VICs.

The proposed approach of this study will help build more robust permafrost datasets and strengthen future permafrost research efforts in mapping permafrost properties and the distribution of excess ice and predicting thaw settlement. It also presents an opportunity to develop methods to extract more information from existing datasets based on an acute understanding of the relations between key physical permafrost properties. The next steps can be followed by improving our understanding and techniques of scanning permafrost as well as using machine-learning-based image segmentation methods to generate datasets and explore the relations between physical permafrost properties.

Author contribution

MR, JP, DF, and JH planned the project; MR, JH, and JP developed the methods; MR, JH, and JP performed the measurements; MR and JH analyzed the data; MR, JP and JH wrote the manuscript draft; MR, JP, JH, and DF reviewed and edited the manuscript.

Competing interests

The authors declare that they have no conflict of interest.

Acknowledgements

The authors would like to thank Evan Francis who helped with sample preparation in earlier experiments. We would also like to thank Nikon Metrology for the support and constructive feedback they provided throughout the project. Casey Buchanan is thanked for collecting the diamict sample used in this study.

Financial support

This research was supported by the NSERC funded Permafrost Partnership Network for Canada (PermafrostNet) and NSERC Discovery grant to Duane Froese. Laboratory infrastructure for the Permafrost Archives Laboratory was funded by Canadian Foundation for Innovation, Government of Alberta, and University of Alberta.

References

Ashi, J., Computed tomography scan image analysis of sediments, in Proc. ODP, Sci. Results, edited by Shipley, T. H., Y. Ogawa, P. Blum, and J. M. Bahr, 156, 151–159, 1997.

Bandara, S., Froese, D. G., St. Louis, V. L., Cooke, C. A., and Calmels, F.: Postdepositional Mercury Mobility in a Permafrost Peatland from Central Yukon, Canada, ACS Earth Sp. Chem., 3, 770–778, https://doi.org/10.1021/acsearthspacechem.9b00010, 2019.

Brown, J., Ferrians, O., Heginbottom, J., and Melnikov, E. S.: Circum-Arctic map of permafrost and ground-ice conditions, https://doi.org/10.3133/cp45, 1997.

Cai, L., Lee, H., Schanke Aas, K., and Westermann, S.: Projecting circum-Arctic excess-ground-ice melt with a sub-grid representation in the Community Land Model, Cryosphere, 14, 4611–4626, https://doi.org/10.5194/tc-14-4611-2020, 2020.

Calmels, F. and Allard, M.: Ice segregation and gas distribution in permafrost using tomodensitometric analysis, Permafr. Periglac. Process., 15, 367–378, https://doi.org/10.1002/ppp.508, 2004.

Calmels, F. and Allard, M.: Segregated ice structures in various heaved permafrost landforms through CT Scan, Earth Surf. Process. Landforms, 33, 209–225, https://doi.org/10.1002/esp.1538, 2008.

Calmels, F., Clavano, W. R., and Froese, D. G.: Progress on X-ray computed tomography (CT) scanning in permfrost studies, in: GeoCalgary 2010 : the 63. Canadian geotechnical conference and 6. Canadian permafrost conference, Calgary, AB (Canada), 12-15 Sep , 1353–1358, 2010.

Crory, F.: Settlement associated with the thawing of permafrost, Hanover, New Hampshire, 599–607 pp., 1973.

Darrow, M. M. and Lieblappen, R. M.: Visualizing cation treatment effects on frozen clay soils through μCT scanning, Cold Reg. Sci. Technol., 175, https://doi.org/10.1016/j.coldregions.2020.103085, 2020.

Duchesne, M. J., Moore, F., Long, B. F., , Labrie, J.: A rapid method for converting medical Computed Tomography scanner topogram attenuation scale to Hounsfield Unit scale and to obtain relative density values. Engineering Geology 103, 100–105, 2009.

Duliu, O.: Computer axial tomography in geosciences: an overview. Earth-Sci. Rev.
48 (4), 265–281, 1999. https://doi.org/10.1016/S0012-8252(99)00056-2

Van Everdingen, R. O.: MULTI-LANGUAGE GLOSSARY of PERMAFROST and RELATED GROUND-ICE TERMS, Calgary, 1998.

Fan, X., Lin, Z., Gao, Z., Meng, X., Niu, F., Luo, J., Yin, G., Zhou, F., Lan, A.: Cryostructures and ground ice content in ice-rich permafrost area of the Qinghai-Tibet Plateau with Computed Tomography Scanning. Journal of Mountain Science. 18. 1208-1221. 10.1007/s11629-020-6197-x, 2021.

French, H. M.: The Periglacial Environment, Wiley, 2007, https://doi.org/10.1002/9781118684931

Flisch, A., and Becker, A.: Industrial X-ray computed tomography studies of lake sediment drill cores. In: Mees, F., Swennen, R., Van Geet, M., Jacobs, P. (Eds.), Applications of X-ray Computed Tomography. Geological Society, London, Special Publication, 215, pp. 205–212, 2003. https://doi.org/10.1144/GSL.SP.2003.215.01.19

French, H., & Shur, Y.: The principles of cryostratigraphy. Earth-Science Reviews, 101(3-4), 190-206, 2010. https://doi.org/10.1016/j.earscirev.2010.04.002

Heiri, O., Lotter, A.F. and Lemcke, G., 2001. Loss on ignition as a method for estimating organic and carbonate content in sediments: reproducibility and comparability of results. Journal of paleolimnology, 25(1), pp.101-110. https://doi.org/10.1023/A:1008119611481.

Hounsfield, G.N.: Computerized transverse axial scanning (tomography). Part I. Description of system. Br. J. Radiol. 46 (552), 1016–1022, 1973. https://doi.org/10.1259/0007-1285-46-552-1016

Johnston, G. H.: Permafrost: engineering design and construction, National Research Council Canada. Associate Committee on Geotechnical Research, 1981.

Kanevskiy, M., Shur, Y., Fortier, D., Jorgenson, M.T., Stephani, E., 2011a. Cryostratigraphy of late Pleistocene syngenetic permafrost (yedoma) in northern Alaska, Itkillik River exposure. Quaternary Research 75, 584–596 http://dx.doi.org/10.1016/j.yqres.2010. 12.003, 2011.

Kanevskiy, M., Shur, Y. L., Connor, B., and Dillon, M. R.: Study of the Ice-Rich Syngenetic Permafrost for Road Design (Interior Alaska), in: Tenth International Conference on Permafrost TICOP, 191–196, 2012.

Ketcham, R. A. and Carlson, W. D.: Acquisition, optimization and interpretation of X-ray computed tomographic imagery: applications to the geosciences, Comput. Geosci., 27, 381–400, https://doi.org/10.1016/S0098-3004(00)00116-3, 2001.

Kokelj, S. V. and Burn, C. R.: Ground ice and soluble cations in near-surface permafrost, Inuvik, Northwest Territories, Canada, Permafr. Periglac. Process., 14, 275–289, https://doi.org/10.1002/ppp.458, 2003.

Kokelj, S. V. and Jorgenson, M. T.: Advances in Thermokarst Research, Permafr. Periglac. Process., 24, 108–119, https://doi.org/10.1002/ppp.1779, 2013.

Kozaki, T., Suzuki, S., Kozai, N., Sato, S., and Ohashi, H.: Observation of Microstructures of Compacted Bentonite by Microfocus X-Ray Computerized Tomography (Micro-CT), J. Nucl. Sci. Technol., 38, 697–699, https://doi.org/10.1080/18811248.2001.9715085, 2001.

Knoll, G.F.: Radiation Detection and Measurement. John Wiley and Sons, New York, 1999.

Kumar and Tiwari: A Comparative Study of Otsu Thresholding and K-means Algorithm of Image Segmentation, Int. J. Eng. Tech. Res. , 9, 2019.

Kyle, J. R. and Ketcham, R. A.: Application of high resolution X-ray computed tomography to mineral deposit origin, evaluation, and processing, Ore Geol. Rev., 65, 821–839, https://doi.org/10.1016/j.oregeorev.2014.09.034, 2015.

Lapalme, C. M., Lacelle, D., Pollard, W., Fortier, D., Davila, A., and McKay, C. P.: Cryostratigraphy and the Sublimation Unconformity in Permafrost from an Ultraxerous Environment, University Valley, McMurdo Dry Valleys of Antarctica, Permafr. Periglac. Process., 28, 649–662, https://doi.org/10.1002/ppp.1948, 2017.

Lin, Z., Gao, Z., Fan, X., Niu, F., Luo, J., Yin, G., and Liu, M.: Factors controlling near surface ground-ice characteristics in a region of warm permafrost, Beiluhe Basin, Qinghai-Tibet Plateau, Geoderma, 376, 114540, https://doi.org/10.1016/j.geoderma.2020.114540, 2020.

Murton, J. B., & French, H. M.: Cryostructures in permafrost, Tuktoyaktuk coastlands, western arctic Canada. Canadian Journal of Earth Sciences, 31(4), 737-747. DOI:10.1139/e94-067, 1994.

Nguyen, T. T. H., Cui, Y.-J., Ferber, V., Herrier, G., Ozturk, T., Plier, F., Puiatti, D., Salager, S., and Tang, A. M.: Effect of freeze-thaw cycles on mechanical strength of lime-treated fine-grained soils, Transp. Geotech., 21, 100281, https://doi.org/10.1016/j.trgeo.2019.100281, 2019.

Nitzbon, J., Westermann, S., Langer, M., Martin, L. C. P., Strauss, J., Laboor, S., and Boike, J.: Fast response of cold ice-rich permafrost in northeast Siberia to a warming climate, Nat. Commun., 11, 2201, https://doi.org/10.1038/s41467-020-15725-8, 2020.

Nitzbon, J., Gadylyaev, D., Schlüter, S., Köhne, J. M., Grosse, G., & Boike, J. (2022). Brief communication: Unravelling the composition and microstructure of a permafrost core using X-ray computed tomography. The Cryosphere, 16, 3507–3515. https://doi.org/10.5194/tc-16-3507-2022

O'Neill, H. B. and Burn, C. R.: Physical and temporal factors controlling the development of near-surface ground ice at Illisarvik, Western Arctic coast, Canada, Can. J. Earth Sci., 49, 1096–1110, https://doi.org/10.1139/E2012-043, 2012.

Object Research Systems. Dragonfly; Object Research Systems: Montreal, QC, Canada, 2021.

Otsu, N.: A Threshold Selection Method from Gray-Level Histograms, IEEE Trans. Syst. Man. Cybern., 9, 62–66, https://doi.org/10.1109/TSMC.1979.4310076, 1979.

Pumple, J., Monteath, A., Harvey, J., Roustaei, M., Alvarez, A., Buchanan, C., & Froese, D. (2024). Non-destructive multi-sensor core logging allows rapid imaging, measurement of bulk density and estimation of ice content in permafrost cores. *EGUsphere*,18,, 489-503. https://doi.org/10.5194/tc-18-489-2024

Pullman, E. R., Jorgenson, M. T., and Shur, Y.: Thaw settlement in soils of the Arctic Coastal Plain, Alaska, Arctic, Antarct. Alp. Res., 39, 468–476, https://doi.org/10.1657/1523-0430(05-045)[PULLMAN]2.0.CO;2, 2007.

Roustaei, M., Pumple, J., Harvey, J., and Froese, D.: Estimating ice and unfrozen water in permafrost samples using industrial computed tomography scanning, in: GeoCalgary 2022, 2022a.

Roustaei, M., Pumple, J., Hendry, M. T., Palat, A., and Froese, D.: Freeze-thaw impacts on macropore structure of fiber-reinforced clay by industrial computed tomography scanning, in: GeoCalgary 2022, 2022b.

Roustaei, M., Pumple, J., Hendry, M. T., J., Harvey, and Froese, D. (2024) : Effect of freeze–thaw cycles on the macrostructure and failure mechanisms of fiber-reinforced clay using industrial computed tomography, Canadian Geotechnical Journal, 00, 1-15, https://doi.org/10.1139/cgj-2023-0136.

Shur, Y. L.: The upper horizon of permafrost soils, in: Proceedings of the Fifth International Conference on Permafrost, 867–871, 1988.

Soret M, Bacharach SL, Buvat I. Partial-volume effect in PET tumor imaging. J Nucl Med. 2007;48:932–945.

Stephani, E., D. Fortier, Y. Shur, R. Fortier, and G. Doré. "A geosys-tems approach to permafrost investigations for engineering applica-tions, an example from a road stabilization experiment, Beaver Creek,Yukon, Canada."Cold Reg. Sci. Technol.100: 20–35.https://doi.org/10.1016/j.coldregions.2013.12.006, 2014.

Subcommittee, P.: Glossary of permafrost and related ground-ice terms. Associate Committee on Geotechnical Research, National Research Council of Canada, Ottawa, 156, 63-64, 1988. https://doi.org/10.1139/e94-067

Tanaka, E. Y., Yoo, J. H., Rodrigues, A. J., Utiyama, E. M., Birolini, D., and Rasslan, S.: A computerized tomography scan method for calculating the hernia sac and abdominal cavity volume in complex large incisional hernia with loss of domain, Hernia, 14, 63–69, https://doi.org/10.1007/s10029-009-0560-8, 2010.

Torrance, J. K., Elliot, T., Martin, R., and Heck, R. J.: X-ray computed tomography of frozen soil, Cold Reg. Sci. Technol., 53, 75–82, https://doi.org/10.1016/j.coldregions.2007.04.010, 2008.

Wang, S., Yang, P., and Yang, Z. (Joey): Characterization of freeze–thaw effects within clay by 3D X-ray Computed Tomography, Cold Reg. Sci. Technol., 148, 13–21, https://doi.org/10.1016/j.coldregions.2018.01.001, 2018.

Wellington, S.L., Vinegar, H.J.: X-ray computerized tomography. J. Pet. Technol. 39 (8), 885–898,1987.

Westermann, S., Langer, M., Boike, J., Heikenfeld, M., Peter, M., Etzelmüller, B., and Krinner, G.: Simulating the thermal regime and thaw processes of ice-rich permafrost ground with the land-surface model CryoGrid 3, Geosci. Model Dev., 9, 523–546, https://doi.org/10.5194/gmd-9-523-2016, 2016.

Zhang, T., Barry, R. G., Knowles, K., Heginbottom, J. A., and Brown, J.: Statistics and characteristics of permafrost and ground-ice distribution in the Northern Hemisphere 1, Polar Geogr., 23, 132–154, https://doi.org/10.1080/10889379909377670, 1999.

546

547

548 **Table 1: Sampling location and physical properties of cores analyzed in the study.**

549

Core ID	Length (cm)	Classification/ Properties	Collection Location/ Depositional Environment	Clay (%)	Silt (%)	Sand (%)
BH18-211	23	Ice-rich silt	Alaska HWY, Yukon, Canada	11	66	23
BH12F-138	16	ice-rich silty peat (top) and ice-poor silt (bottom)	Alaska HWY, Yukon, Canada	top 8 bottom 12	top 52 bottom 57	top 40 bottom 31
BS19-3-6	19	Diamicton	Dempster HWY, Yukon, Canada	18	51	31
BH20B-337	20	Ice-poor silt	Alaska HWY, Yukon, Canada	8	67	25
DH13-589	26	Ice-rich homogenous peat.	Dempster HWY, Yukon, Canada	N/A	N/A	N/A

550

551

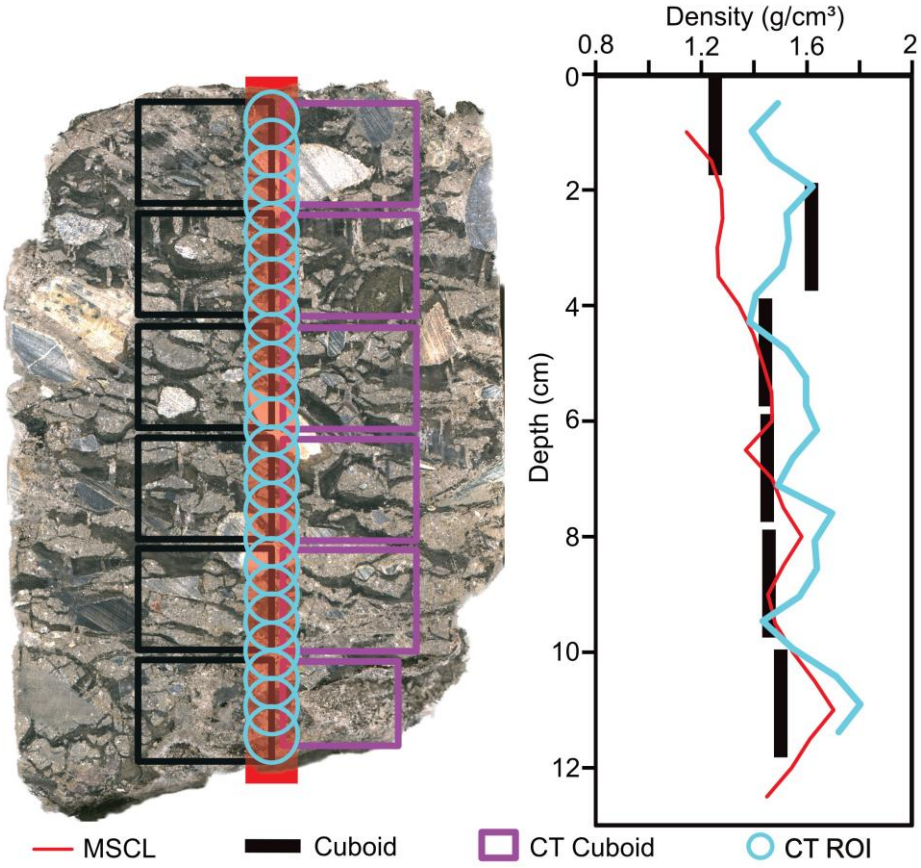

Figure 1: Image of a core highlighting the destructive subsample locations relative to the non-destructive data collection transects (black: subsampled cubes for destructive measurements, purple: subsampled cubes for CT scans)

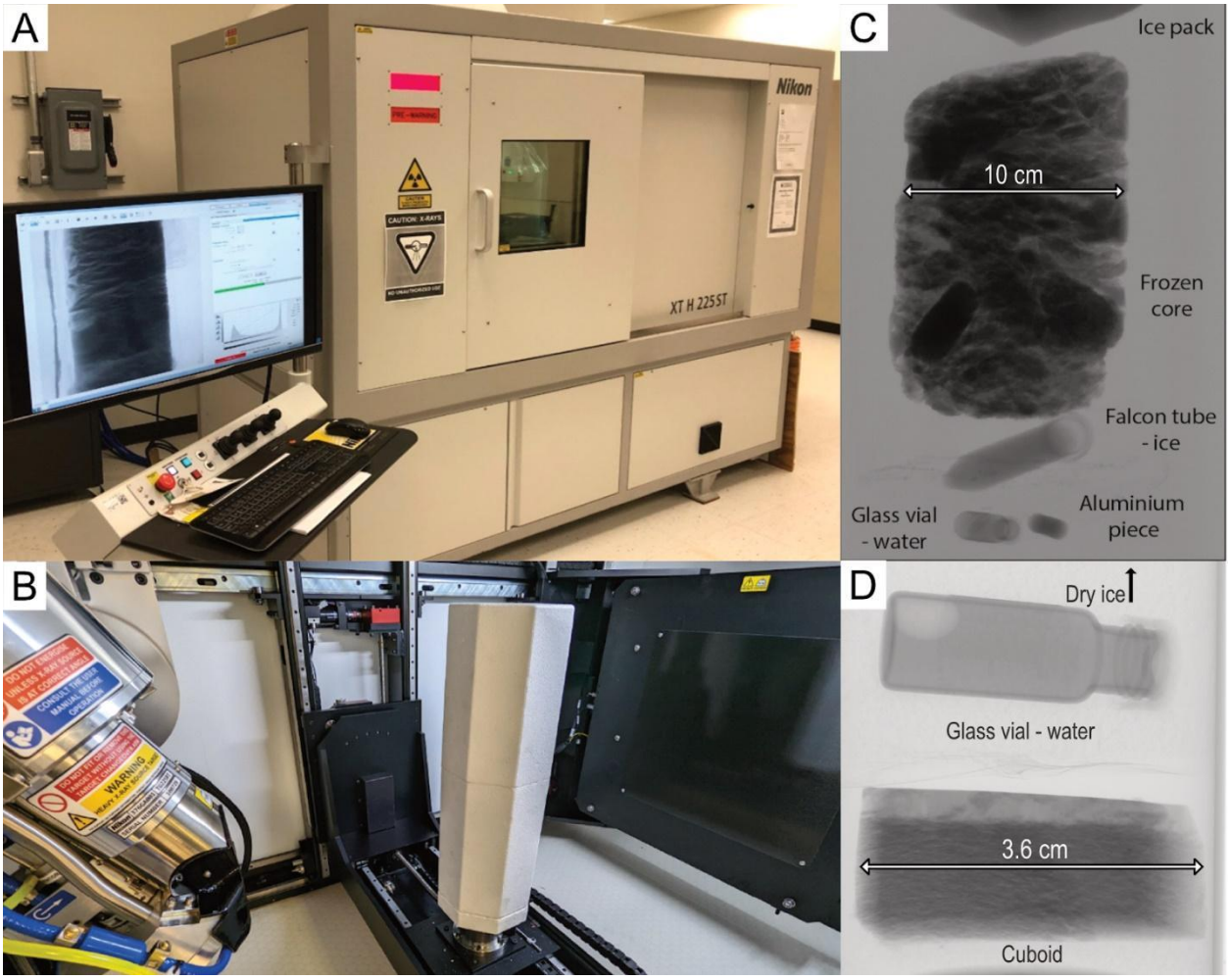

Figure 2: (A) The CT scanner of the PACS Lab.(B) The internal setup for the core scan. (C) X-ray image of the internal setup of the core (D) X-ray image of the internal setup of the cube.

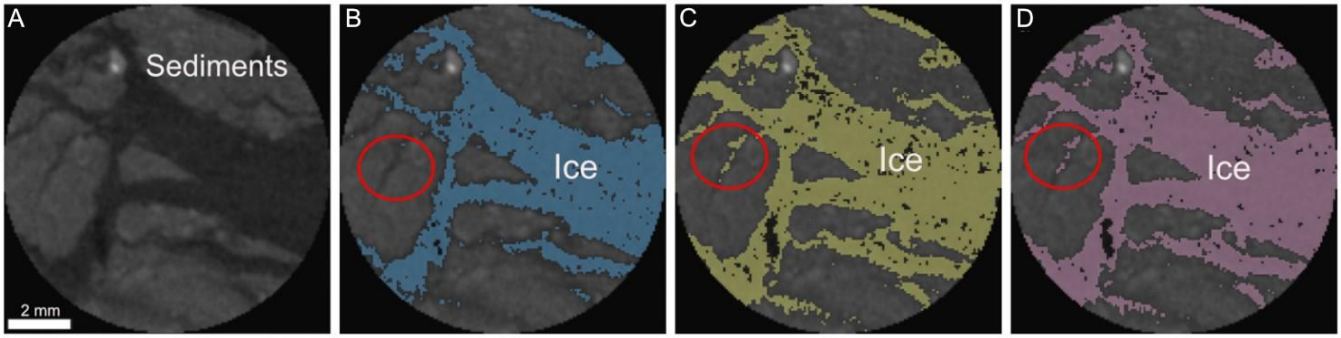

Figure 3: Overview of a slice from ice rich silt core (A) before image processing (B) after the first step, (C) after the second step, and (D) after the third step of image processing using the Otsu method.

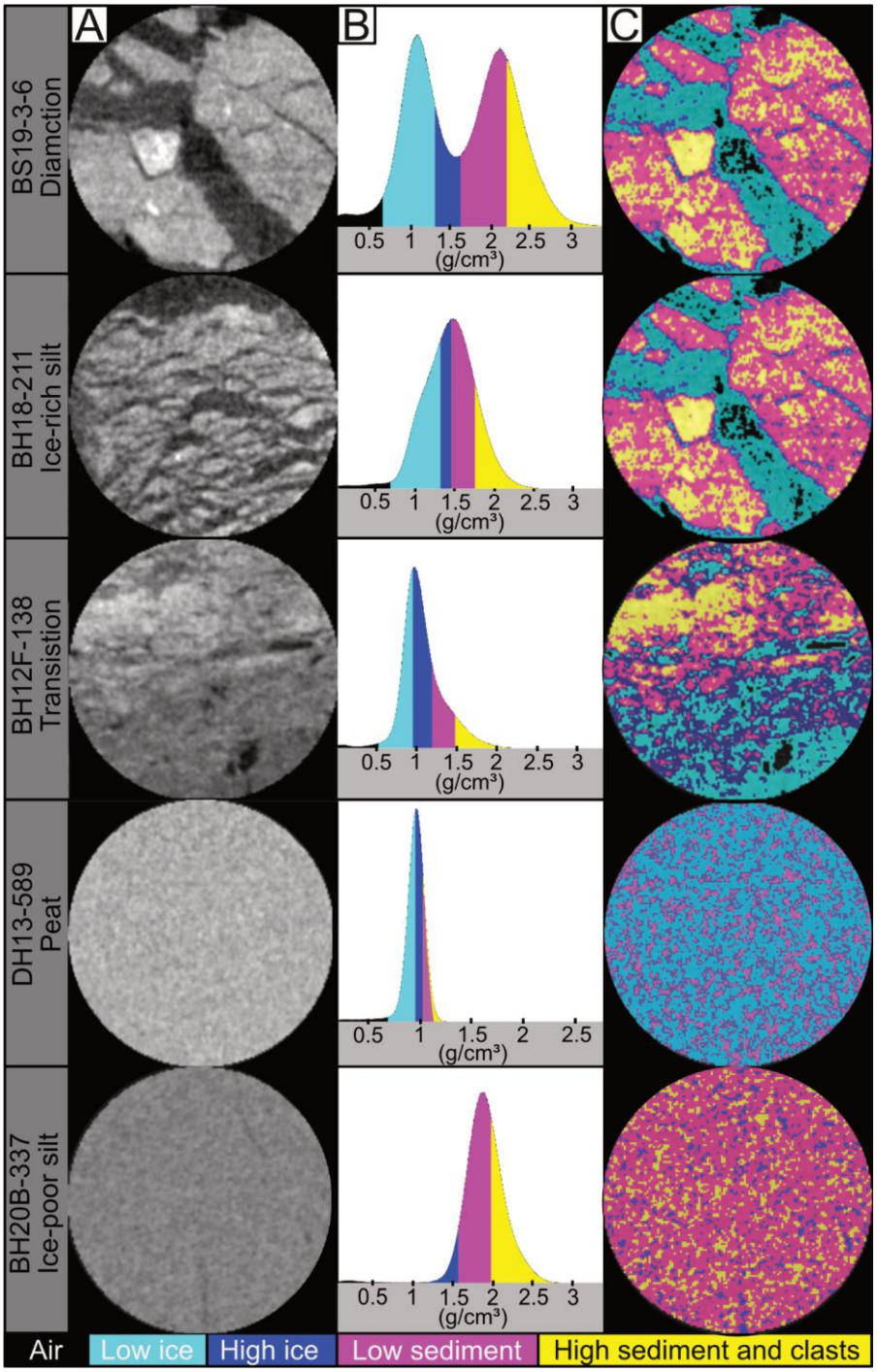

Figure 4: (A) overview of slices from the permafrost cores before image processing (B) histograms, and (C) image segmentation results

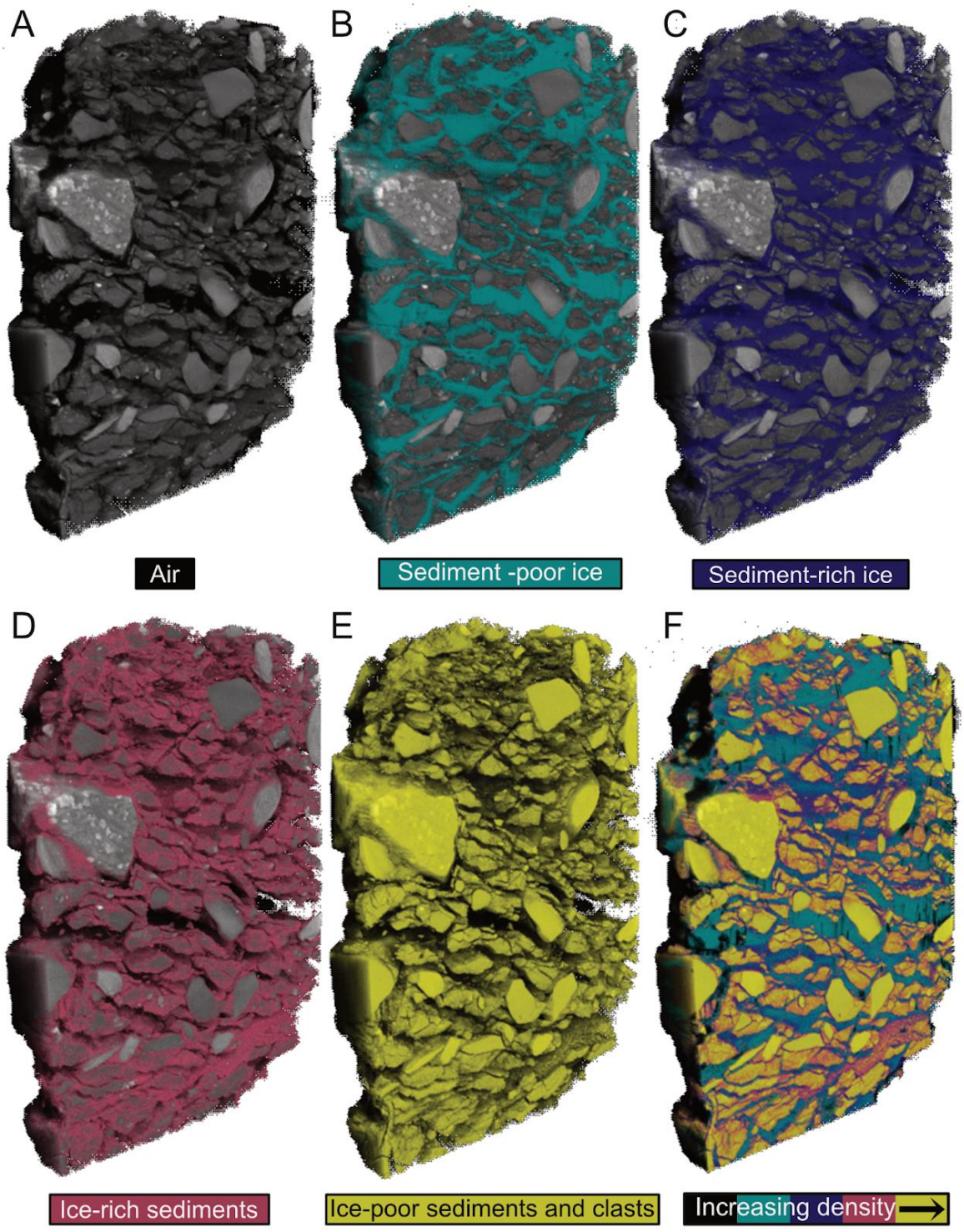

Figure 5: Image segmentation results of the diamicton core.

Table 2: Root mean square error results for the comparison between the CT, Cuboid and MSCL VIC, EIC and density results.

Core ID	RMSE Density CT vs Cuboid (g/cm^3)	RMSE VIC CT vs Cuboid (%)	RMSE VEIC CT vs Cuboid (%)	RMSE Density CT vs Geotek (g/cm^3)	RMSE VIC CT vs Geotek (%)
BS19-3-6	0.14	3	8	0.14	4
BH18-211	0.12	7	9	0.05	8
DH13-589	0.05	1	4	0.03	4
BH12F-138 (top)	0.07	3	7	0.02	11
BH12F-138 (bottom)	0.19	3	2	0.10	10
BH12F-138 (whole core)	0.13	3	5	0.06	10
BH20B-337	0.14	3	5	0.14	3
Overall average	0.12	3	6	0.08	7

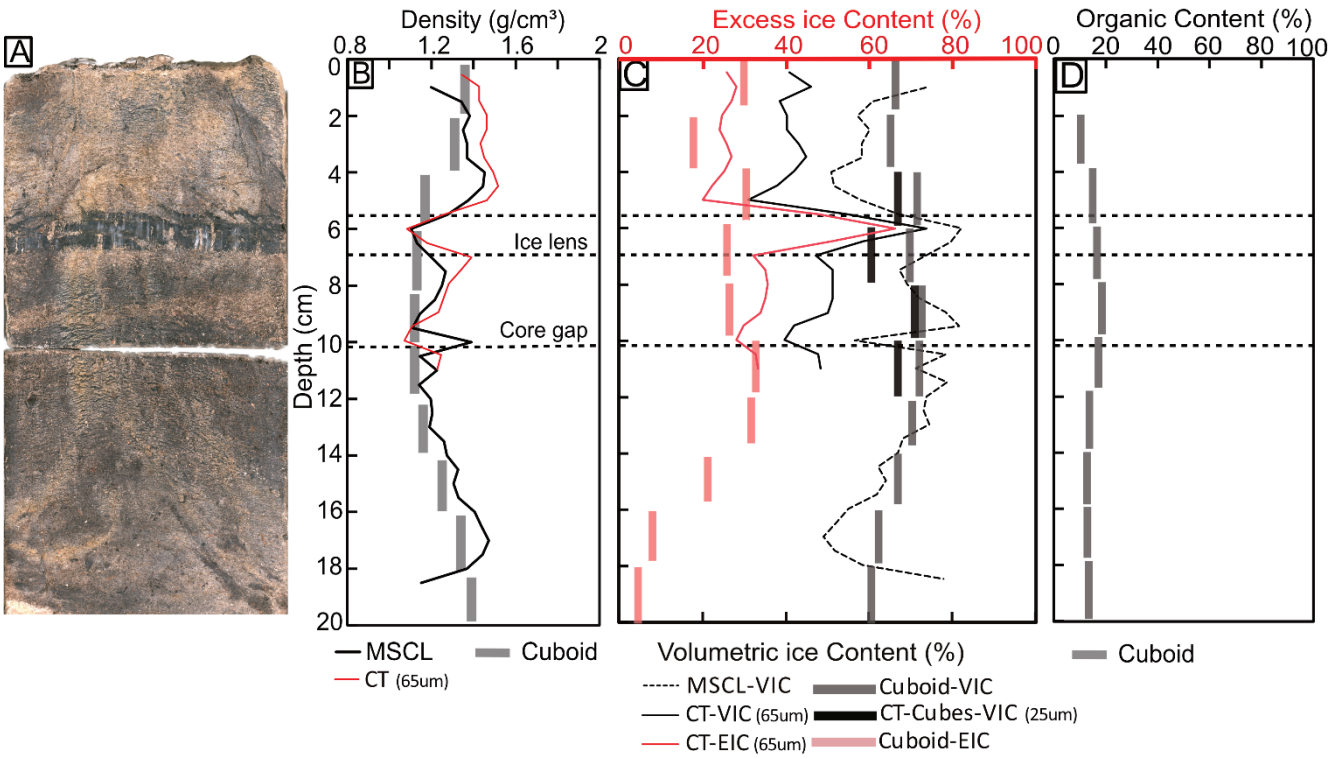

Figure 6: (A) MSCL image of the ice-rich, organic-rich silt core; (B) bulk density; (C) ice contents; (D) organic content distribution in core depth; (E) black and white image of MSCL image with ice highlighted in black.

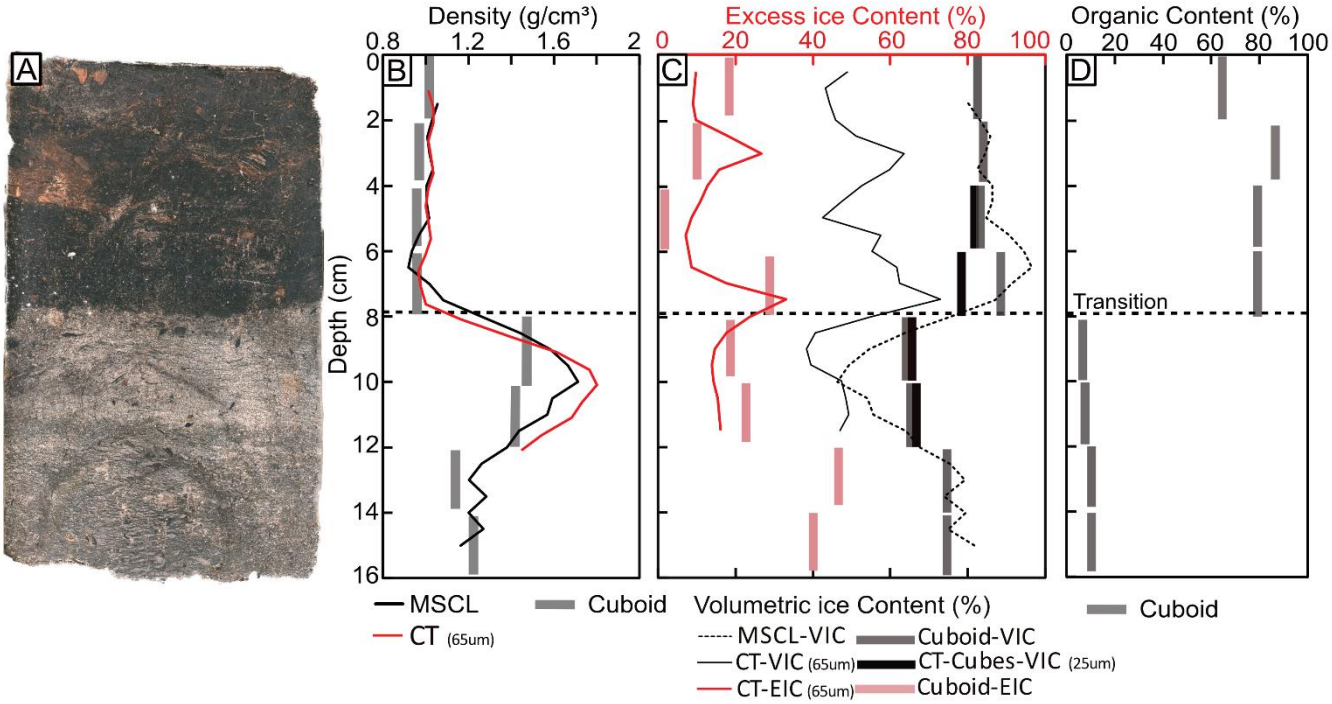

577

578 **Figure 7: (A) MSCL image of the transition core; (B) bulk density; (C) ice contents; (D) organic content distribution in core depth;**
579 **(E) black and white image of MSCL image with ice highlighted in black.**

580

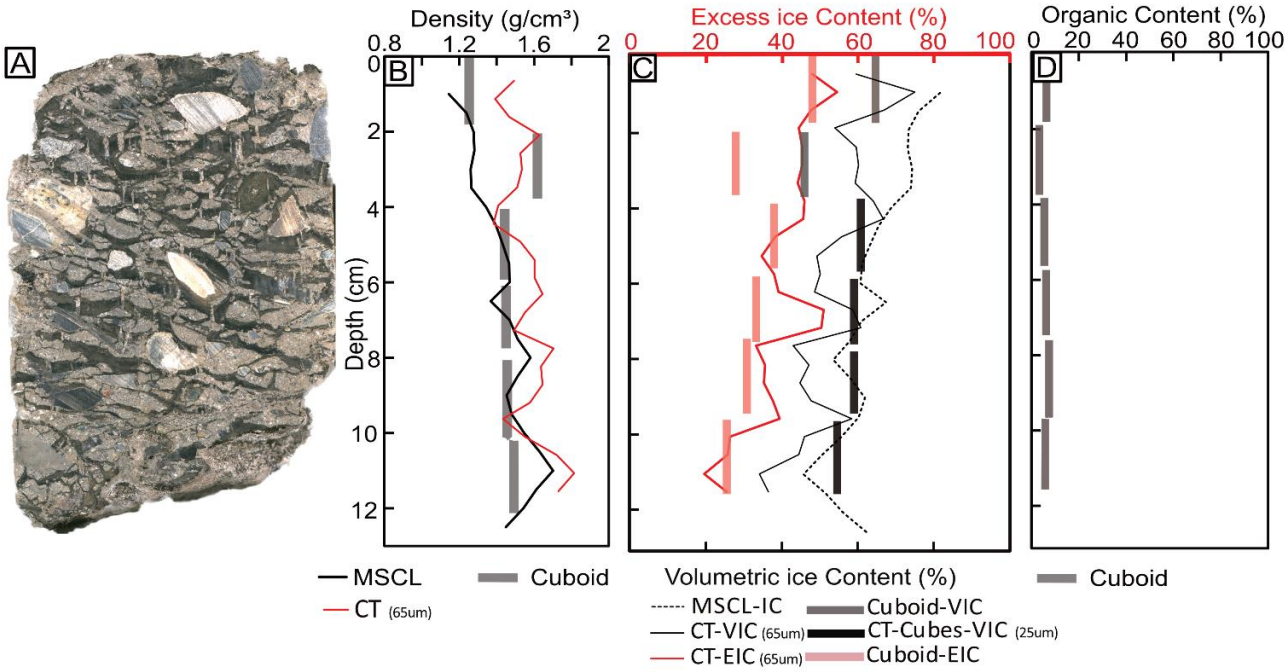

581

582 **Figure 8: (A) MSCL image of the diamicton core; (B) bulk density; (C) ice contents; (D) organic content distribution in core depth;**
583 **(E) black and white image of MSCL image with ice highlighted in black.**

584

585

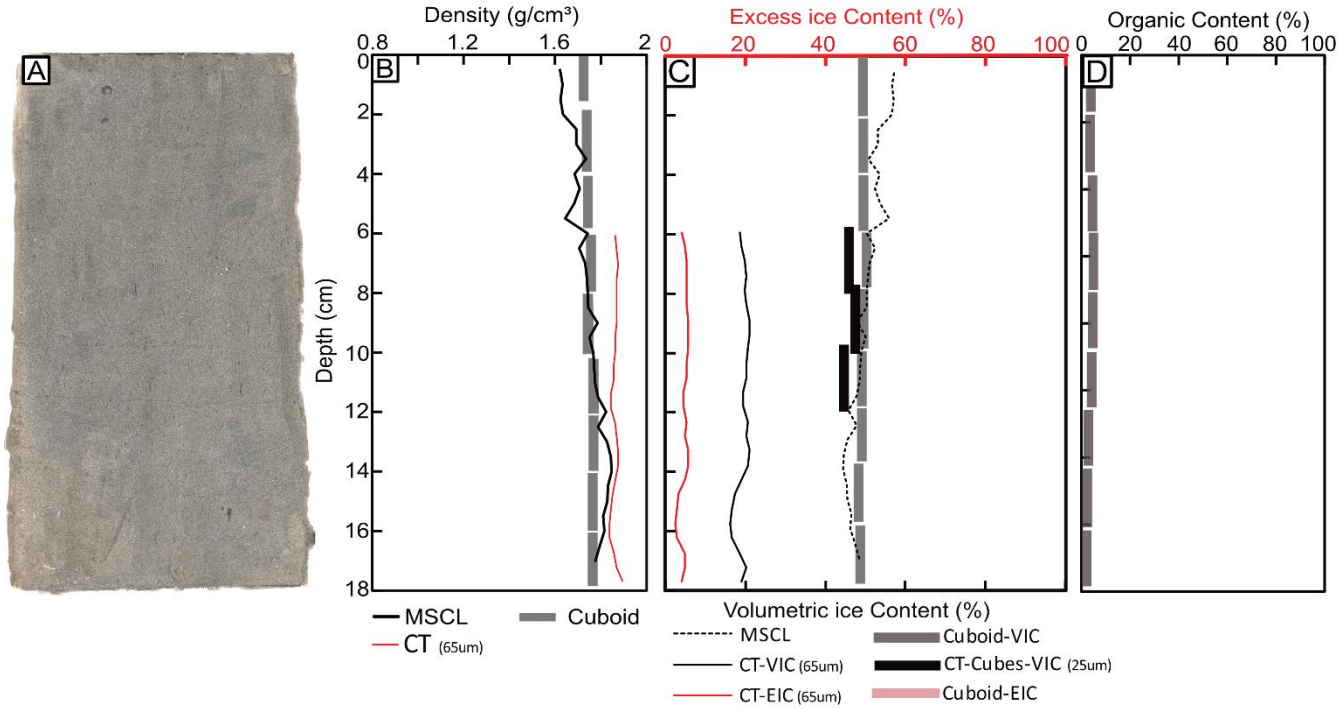

586

587 **Figure 9: (A) MSCL image of the ice-poor silt core; (B) bulk density; (C) ice contents; (D) organic content distribution in core depth;**
588 **(E) black and white image of MSCL image with ice highlighted in black.**

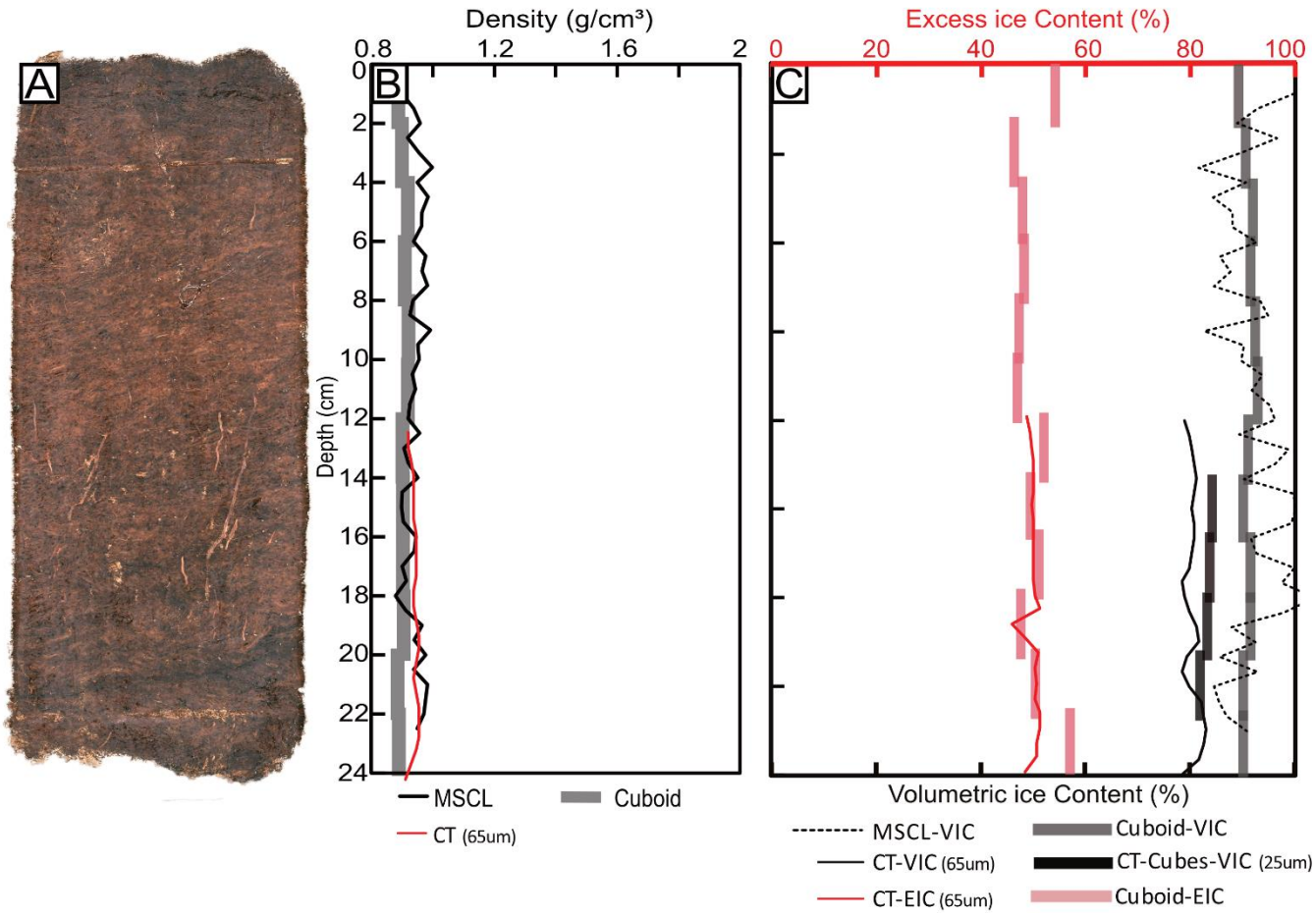

589

590 **Figure 10: (A) MSCL image of the peat core; (B) bulk density; (C) ice contents; (D) organic content distribution in core depth; (E)**
591 **black and white image of MSCL image with ice highlighted in black.**

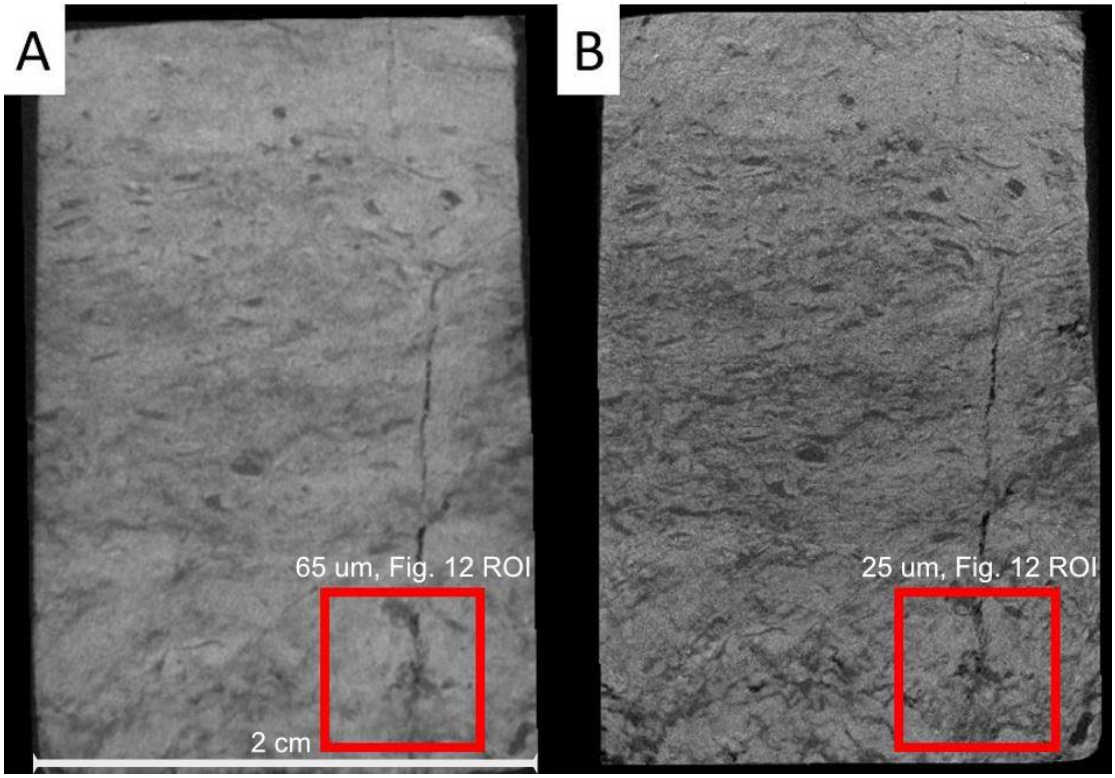

Figure 11: CT images of a cube (BH12F-138-10-12 cm) from the transition core at 65 µm (A) and 25 µm (B).

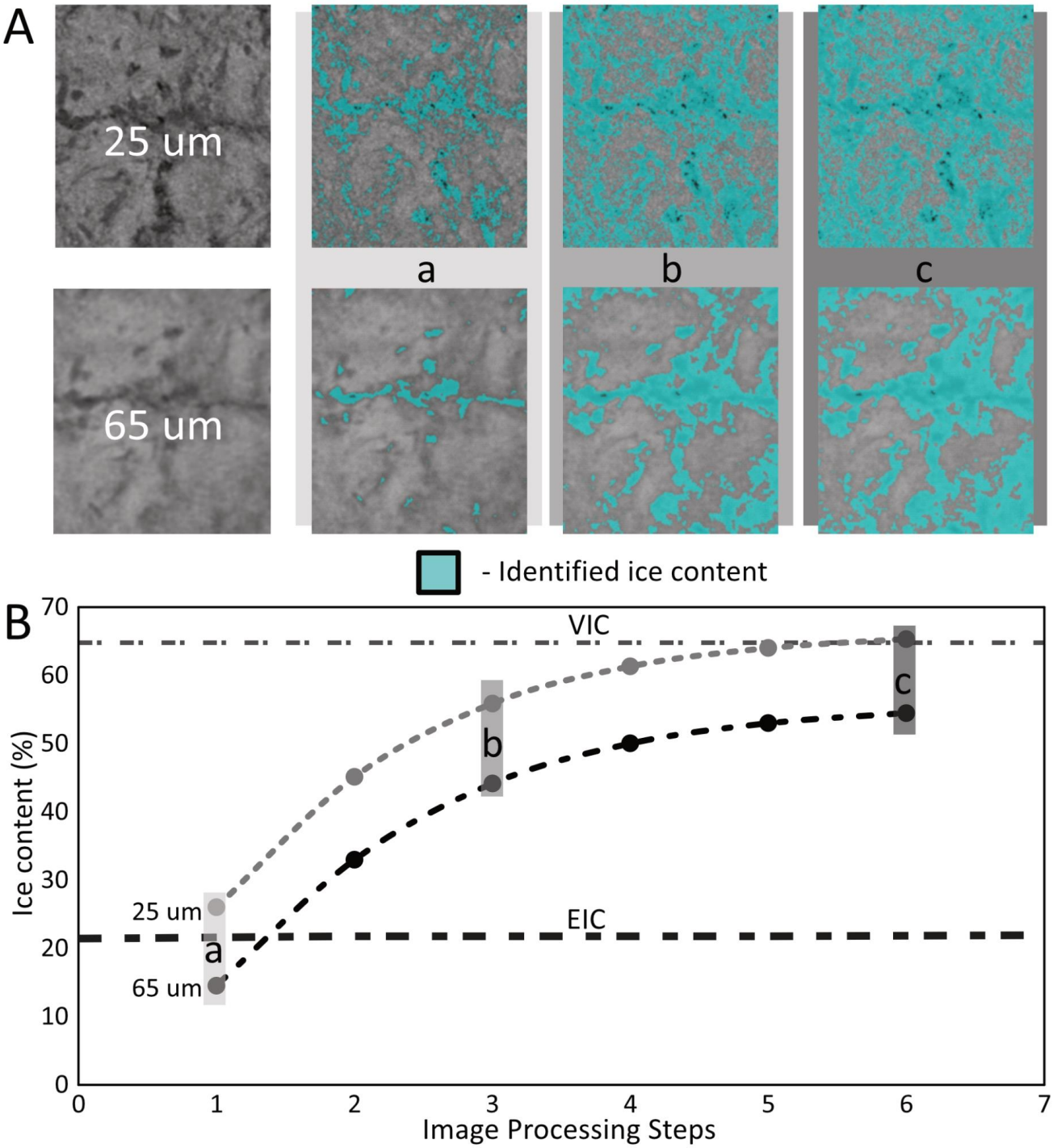

Figure 12: (A) CT ROI's taken from the 65 µm and 25 µm cube scans (BH12F-138-10-12 cm), (B) Identified ice contents at each image processing step using the Otsu split method.

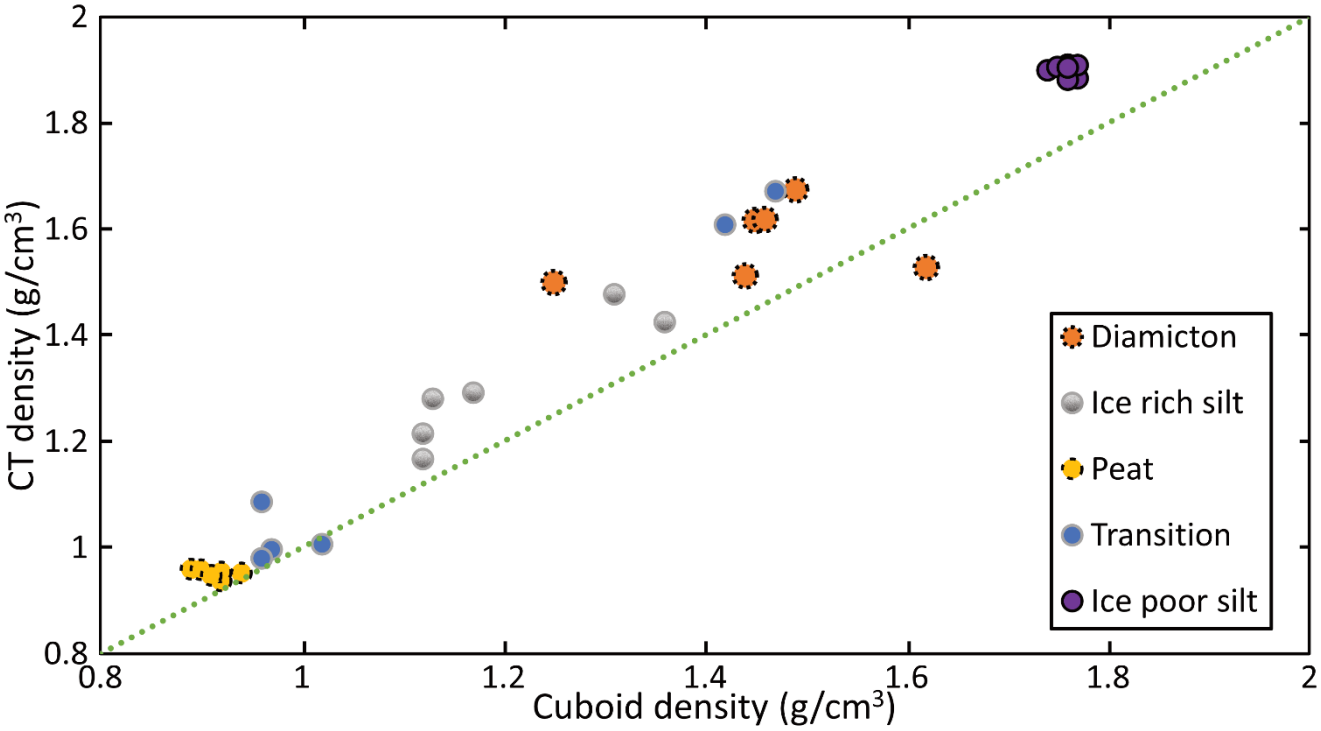

Figure 13: Estimated densities from CT image processing vs calculated ones from cuboid method.

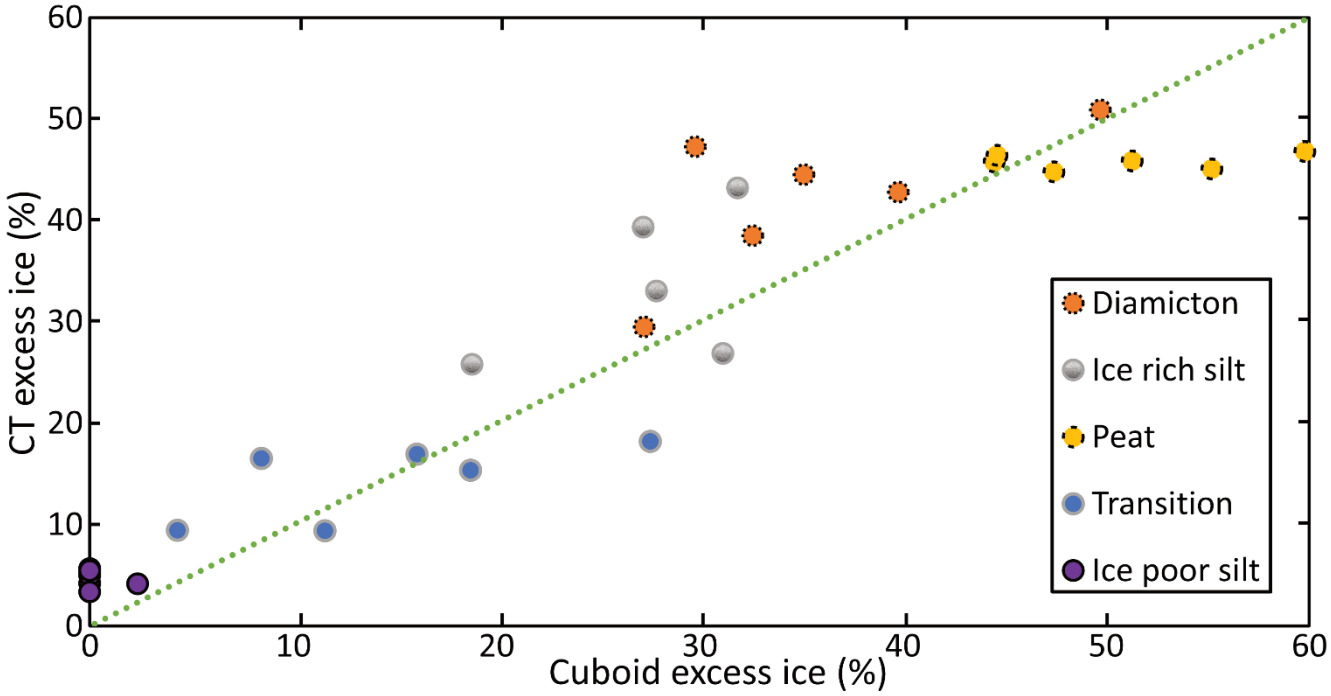

Figure 14: Estimated excess ice contents from CT image processing vs calculated values from cuboid method.

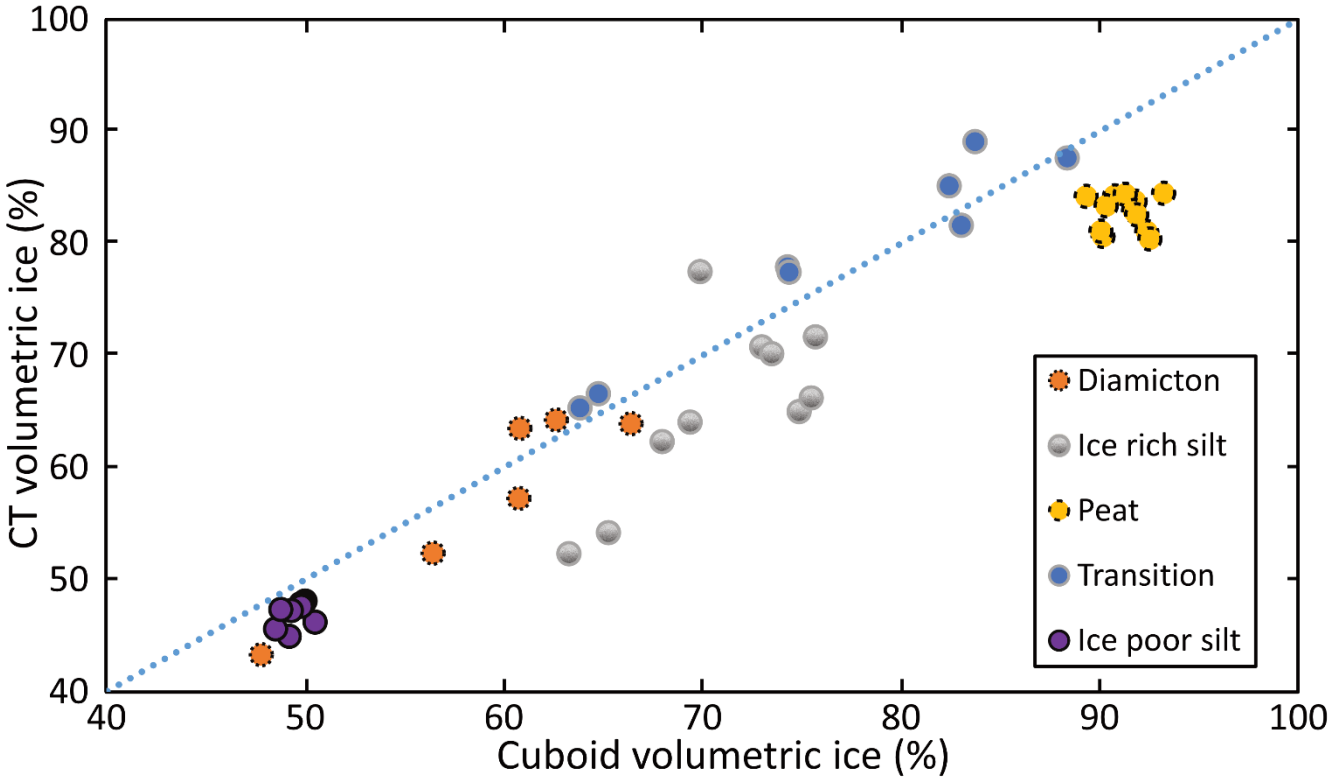

Figure 15: Estimated volumetric ice contents from CT image processing vs calculated values from cuboid method.

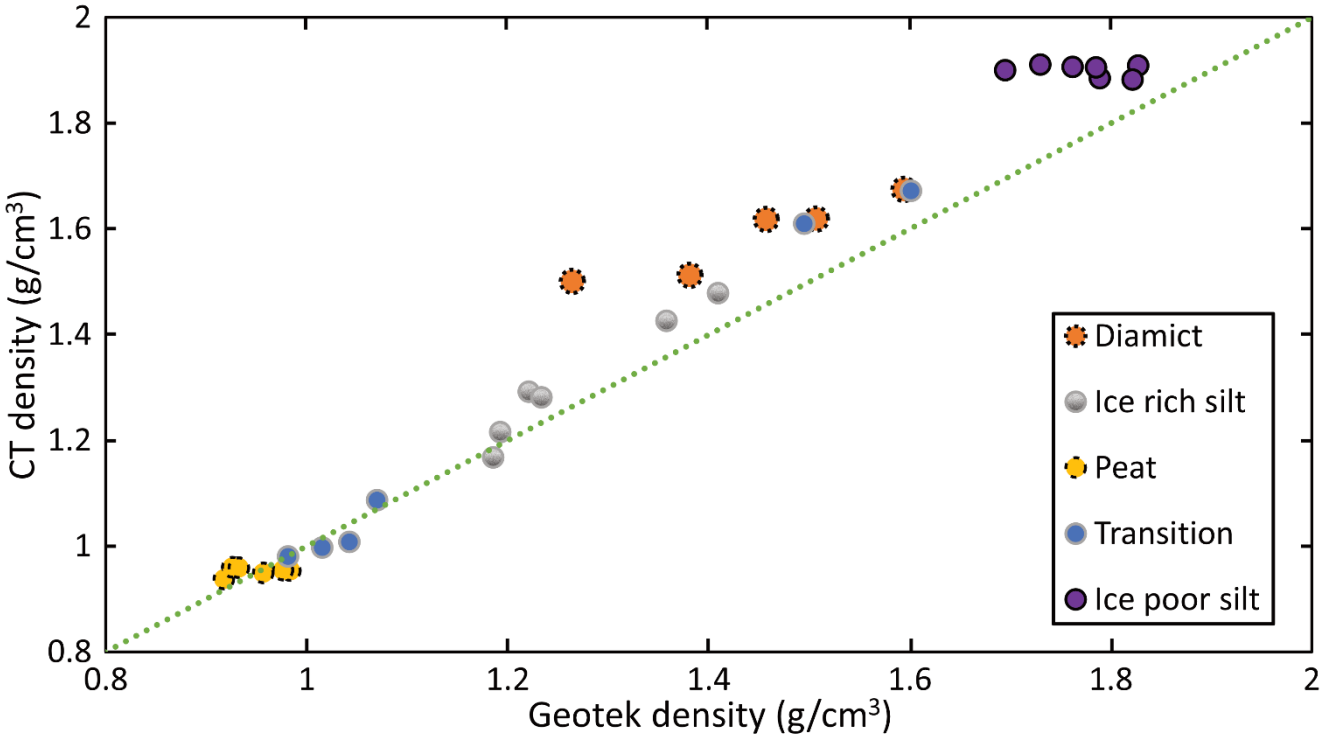

Figure 16: Estimated bulk density from CT image processing vs calculated values from MSCL method.

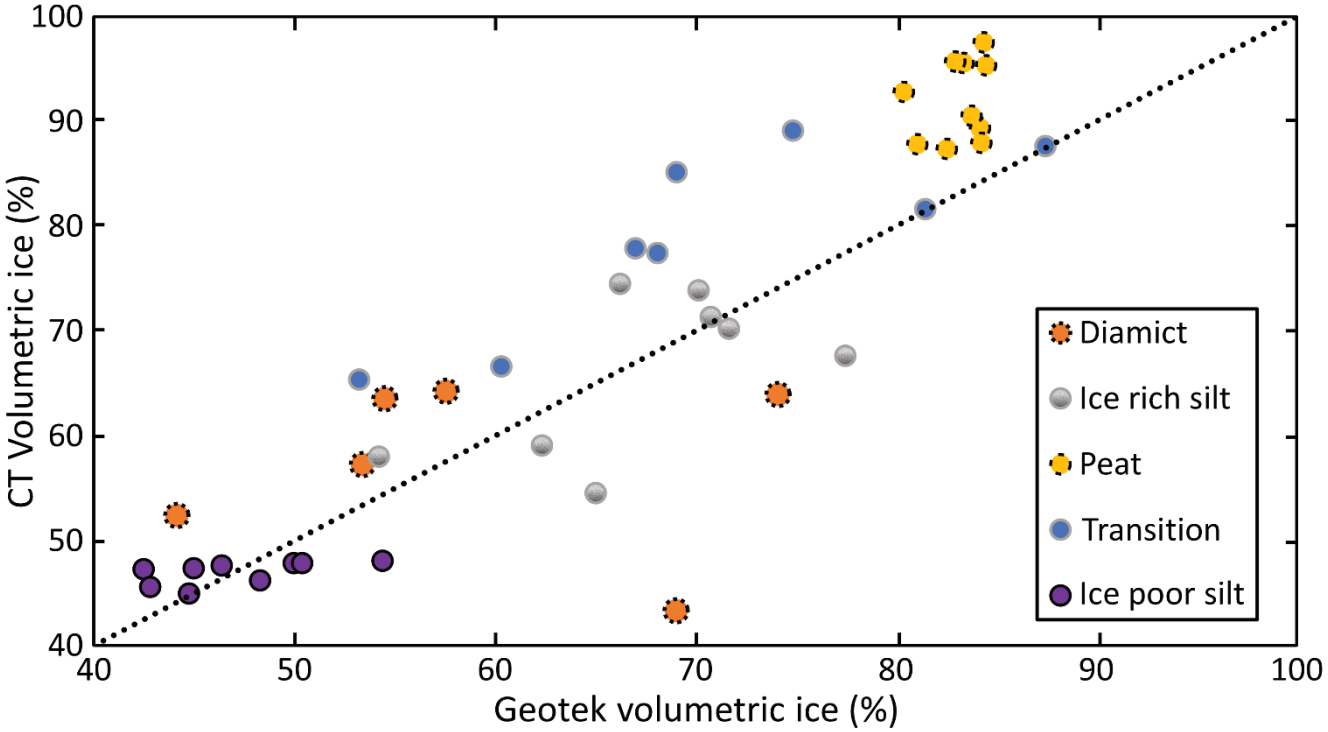

606

607 **Figure 17: Estimated volumetric ice contents from CT image processing vs calculated values from MSCL method.**

608